

A NEW LOOK AT THE KINEMATICS OF NEUTRAL HYDROGEN IN THE SMALL MAGELLANIC CLOUD

S. STANIMIROVIĆ

Radio Astronomy Lab, UC Berkeley, 601 Campbell Hall, Berkeley, CA 94720
sstanimi@astro.berkeley.edu

L. STAVELEY-SMITH

Australia Telescope National Facility, CSIRO, P.O. Box 76, Epping, NSW 1710, Australia

P. A. JONES

Australia Telescope National Facility, CSIRO, P.O. Box 76, Epping, NSW 1710, Australia

To appear in ApJ, 2004 March 20

ABSTRACT

We have used the latest HI observations of the Small Magellanic Cloud (SMC), obtained with the Australia Telescope Compact Array and the Parkes telescope, to re-examine the kinematics of this dwarf, irregular galaxy. A large velocity gradient is found in the HI velocity field with a significant symmetry in iso-velocity contours, suggestive of a differential rotation. A comparison of HI data with the predictions from tidal models for the SMC evolution suggests that the central region of the SMC corresponds to the central, disk- or bar-like, component left from the rotationally supported SMC disk prior to its last two encounters with the Large Magellanic Cloud. In this scenario, the velocity gradient is expected as a left-over from the original, pre-encounter, angular momentum. We have derived the HI rotation curve and the mass model for the SMC. This rotation curve rapidly rises to about 60 km s^{-1} up to the turnover radius of $\sim 3 \text{ kpc}$. A stellar mass-to-light ratio of about unity is required to match the observed rotation curve, suggesting that a dark matter halo is not needed to explain the dynamics of the SMC. A set of derived kinematic parameters agrees well with the assumptions used in tidal theoretical models that led to a good reproduction of observational properties of the Magellanic System. The dynamical mass of the SMC, derived from the rotation curve, is $2.4 \times 10^9 M_{\odot}$.

Subject headings: galaxies: interactions – galaxies: structure – Magellanic Clouds – galaxies: kinematics and dynamics

1. INTRODUCTION

The Small Magellanic Cloud (SMC) is a nearby¹, gas-rich, dwarf irregular galaxy. Its morphology, dynamics, and evolution are highly complex, and must have been heavily influenced by gravitational interactions with the nearby Large Magellanic Cloud (LMC) and the Galaxy (Putman et al. 1998). As a dwarf irregular galaxy, the SMC is different from our own Galaxy in many respects, having a lower heavy element abundance, significantly lower dust content, and a consequently stronger interstellar radiation field (Stanimirović et al. 1999; Stanimirović & Lazarian 2001).

Many recent high resolution studies have shown that dwarf galaxies in general have a very dynamic interstellar medium (ISM), structured mainly by star formation and its aftermath. The most obvious example of star-formation creativity are numerous expanding shells of gas (Puche et al. 1992; Staveley-Smith et al. 1997; Kim et al. 1999; Stanimirović et al. 1999; Walter 1999). Dwarf galaxies are also usually found to have large, and dynamically important, halos of dark matter (Mateo 1998). The relative roles of a galactic rotation, pressure support, dark matter, and magnetic fields on the 3-D structure and dynamics of these galaxies are still open questions. Furthermore, it is not clear yet whether different stages of galactic evolution are marked by fundamentally different phenomena, and whether these phenomena are selective with respect

to spatial scales.

It has been known for some time that the morphology and kinematics of the SMC traced by different stellar populations show very different properties (Gardiner & Hatzidimitriou 1992). This has been one of the major reasons to start thinking about forces other than gravitational that may have played a significant role in the formation and evolution of the whole Magellanic System. The questions of morphology and kinematics are closely related to the long-standing and greatly controversial questions of the SMC's 3-D structure and depth along the line-of-sight. As the results of several new optical and near-IR surveys are becoming available (Zaritsky et al. 2000; Cioni et al. 2000; Maragoudaki et al. 2001), revealing structural evolution of the SMC, as well as new N-body simulations of the dynamical evolution of the SMC (Yoshizawa & Noguchi 2003), we find that it is timely to re-examine the morphology and kinematics of the SMC as traced by the neutral hydrogen (HI).

The mapping of HI in the SMC has a long and productive history. After the pioneering work by Kerr et al. (1954) and Hindman et al. (1963), Hindman (1967) was the first to notice the velocity gradient in the SMC and to model its rotation curve, followed by Bajaja & Loiseau (1982). However, the velocity field of the SMC is far from a simple text-book example. The HI profiles, often complex and with multiple peaks, have caused much controversy in the past, being interpreted as due to either expanding

¹ Throughout this paper we assume a distance to the SMC of 60 kpc (Westerlund 1997).

shells of gas or spatially separate systems (Hindman 1967; Mathewson et al. 1988; Martin et al. 1989). An improvement by a factor of ten in spatial resolution, relative to previous surveys with the Parkes telescope, was achieved in the HI survey by Staveley-Smith et al. (1997), using the Australia Telescope Compact Array (ATCA). These new high resolution data showed that much of the HI profile complexity lies in the huge number (~ 500) of expanding shells. The new high resolution HI observations were complemented with new low resolution observations obtained with the Parkes telescope to provide information over a continuous range of spatial scales from 30 pc to 4 kpc (Stanimirović et al. 1999).

The aim of this paper is to re-examine the HI kinematics of the SMC, as viewed from high resolution observations, and compare it with predictions from tidal theoretical models. We start by summarizing the HI observations in Section 2. The morphology and kinematics of the SMC from the HI distribution, as well as viewed using other tracers, are discussed in Section 3. The SMC 3-D structure and line-of-sight depth are reviewed briefly in Section 4. We then compare HI data with predictions from several tidal models in Section 5. The rotation curve and mass model of the SMC are investigated in Section 6. Finally, a summary and concluding remarks are given in Section 7.

2. HI DATA

The HI in the SMC was observed with the ATCA², a radio interferometer, in a mosaicing mode (Staveley-Smith et al. 1997). Observations of the same area were obtained also with the 64-m Parkes telescope. The two sets of observations were then combined (Stanimirović et al. 1999), resulting in the final HI data cube with angular resolution of 98 arcsec, velocity resolution of 1.65 km s^{-1} , and $1-\sigma$ brightness-temperature sensitivity of 1.3 K to the full range of spatial scales between 30 pc and 4 kpc. The area covered with these observations is RA $00^{\text{h}}30^{\text{m}}$ to $01^{\text{h}}30^{\text{m}}$ and Dec -71° to -75° (J2000), over a velocity range of 90 to 215 km s^{-1} . For details about the ATCA and Parkes observations, data processing, and data combination (short-spacings correction) see Staveley-Smith et al. (1997) and Stanimirović et al. (1999).

3. STRUCTURE AND KINEMATICS OF THE SMC

3.1. HI distribution

Fig. 1 shows the integrated HI column-density distribution. The large-scale HI morphology of the SMC is quite irregular and does not show obvious symmetry. The most prominent features are the elongation from the north-east to the south-west and the V-shaped concentration at the east (RA $01^{\text{h}} 14^{\text{m}}$, Dec $-73^\circ 15'$, J2000). These are usually referred to as the ‘bar’ and the Eastern Wing, although their dynamical importance is still not well understood. A ‘bridge’ of gas appears to connect the ‘bar’ and the Wing (note that this is not the Magellanic Bridge that connects the SMC and the LMC), while the arm-like extension of the ‘bar’ towards the north-east is also prominent. On smaller scales and looking at different velocity channels (see Stanimirović et al. 1999), the HI distribution appears very complex and frothy, being dominated

by numerous expanding shells, filaments and arcs. The total estimated mass of the HI, after correction for self-absorption, is $4.2 \times 10^8 M_\odot$ (Stanimirović et al. 1999). A summary of radio and optical properties of the SMC is given in Table 1.

The HI column density distribution is super-imposed on the V-band optical image of the SMC, kindly provided to us by M. Bessell, in Fig. 2. In general, in the ‘bar’ and the Eastern Wing the stellar and HI distributions correlate well, however the HI is significantly more extended towards the south-west, the south-east, and the north-west.

3.2. HI kinematics

The intensity-weighted mean velocity along each line-of-sight, or the first moment map, was derived from the full resolution HI data cube (corrected for short spacings), and is shown in Fig. 3. A large velocity gradient, from 91 km s^{-1} in the south-west to 200 km s^{-1} in the north-east, can be seen. The iso-velocity contours show some large-scale symmetry suggestive of differential rotation for the main gaseous body of the SMC. However, clear distortions are visible in the north-west, most likely corresponding to several shells and filamentary features aligned into a chimney-like structure at velocity $\sim 123 \text{ km s}^{-1}$ (Fig. 2 in Stanimirović et al. 1999), and in the south-east, towards the Eastern Wing region, where again a supergiant shell was found (494A; see Stanimirović et al. 1999). These perturbations form a S-shaped feature perpendicular to the direction of the main velocity gradient (as shown in Fig. 3 with a dashed line).

The second moment map or the intensity-weighted velocity dispersion is shown in Fig. 4. This velocity dispersion varies from ~ 5 to 40 km s^{-1} across the SMC. The regions with higher dispersion appear to be associated with the positions of the three largest supergiant shells (SGSs). The region around RA $01^{\text{h}} 00^{\text{m}}$, Dec $-71^\circ 30'$ (J2000) has the lowest dispersion with a mean value of $\sim 10 \text{ km s}^{-1}$. As this region corresponds to the receding hemisphere of the SGS 304A (Stanimirović et al. 1999), the lower velocity dispersion may be explained with the fact that most of the approaching hemisphere of SGS 304A is missing at the northside.

We have investigated two effects that could significantly influence the observed velocity field shown in Fig. 3: (i) the effect of the proper motion of the SMC, and (ii) the effect of multiple-peak velocity profiles.

(i) The binary motion of the SMC around the Galaxy, combined with its large angular extent, could have a significant contribution to the observed velocity field, as was shown for the case of the LMC by Luks & Rohlfs (1992) and Kim et al. (1998). This contribution consists of the projection of the transverse velocity of the SMC’s center of gravity on the line-of-sight at each position. In the case of a large angular extent on the sky, this projection can vary greatly across the field of observation and cause a significant change in the observed velocity field. To correct for this effect, we used values for the SMC’s proper motion and the heliocentric transversal velocity predicted by numerical simulations by Gardiner et al. (1994), which are in agreement with the estimates based on a combination of proper motion measurements by Kroupa et al.

² The Australia Telescope is funded by the Commonwealth of Australia for operation as a National Facility managed by CSIRO.

TABLE 1
RADIO AND OPTICAL PROPERTIES OF THE SMC.

Property	Value
Radio:	
<i>Measured:</i>	
RA (J2000) ^a	01 ^h 05 ^m
Dec (J2000) ^a	−72° 25′
Systemic velocity ^b , V_{sys} (Gal.)	24 km s ^{−1}
Systemic velocity ^b , V_{sys} (Hel.)	160 km s ^{−1}
HI mass ^c , M_{HI}	$4.2 \times 10^8 M_{\odot}$
<i>Model-dependent:</i>	
Inclination ^d , i	$40^{\circ} \pm 20^{\circ}$
Kinematic Position angle ^d , PA	40°
V_{max}^d	60 km s ^{−1}
R_{max}^d	2.5 – 3 kpc
M_{dyn}^d	$2.4 \times 10^9 M_{\odot}$
Optical:	
Extinction ^e , E_{B-V}	~ 0.05–0.25 mag
Total visible magnitude ^f , V_{T}	+2.4 mag
Absolute visible magnitude ^f , M_{V}	−16.5
Visible luminosity ^f , L_{V}	$3.1 \times 10^8 L_{\odot}$
$M_{\text{H}}/L_{\text{V}}$	$1.4 M_{\odot}/L_{\odot}$
$(B - V)_{\text{T}}^0$	0.41
$(U - B)_{\text{T}}^0$	−0.23

^aThe apparent kinematic center derived as the intersection of the principal kinematic axes.

^bSystemic velocity of the apparent kinematic center derived from the velocity field.

^cStanimirović et al. (1999).

^dDerived from the tilted ring analysis in Section 6.

^eZaritsky et al. (2002).

^fde Vaucouleurs et al. (1991).

FIG. 1.— [f1.jpeg] An HI column-density image of the SMC. The grey-scale intensity range is 0 to 7×10^{21} atoms cm^{−2} with a linear transfer function. The maximum HI column density, 1.43×10^{22} atoms cm^{−2}, is at position RA 00^h47^m33^s, Dec −73°05′26″ (J2000).

FIG. 2.— [f2.jpeg] The HI column density image super-imposed on the V-band CCD image. The contour levels range from 2.0×10^{20} to 1.3×10^{22} atoms cm^{−2}, with a contour interval of 3.8×10^{20} atoms cm^{−2}. The V-band image was obtained by Mike Bessell using the 16″ telescope at the Mount Stromlo Observatory.

FIG. 3.— [f3.jpeg] The intensity-weighted mean heliocentric velocity field of the SMC, derived from the combination of the ATCA and Parkes data. The grey scale range is 120 to 200 km s^{−1} with a linear transfer function. The contour levels range from 120 to 200 km s^{−1}, with a contour interval of 10 km s^{−1}. All pixels with a corresponding HI column density lower than 9×10^{20} atoms cm^{−2} were masked out. The direction of the largest velocity gradient is shown with a solid line, and the direction of the largest velocity distortions, forming a S-shaped features, is shown with a dashed line.

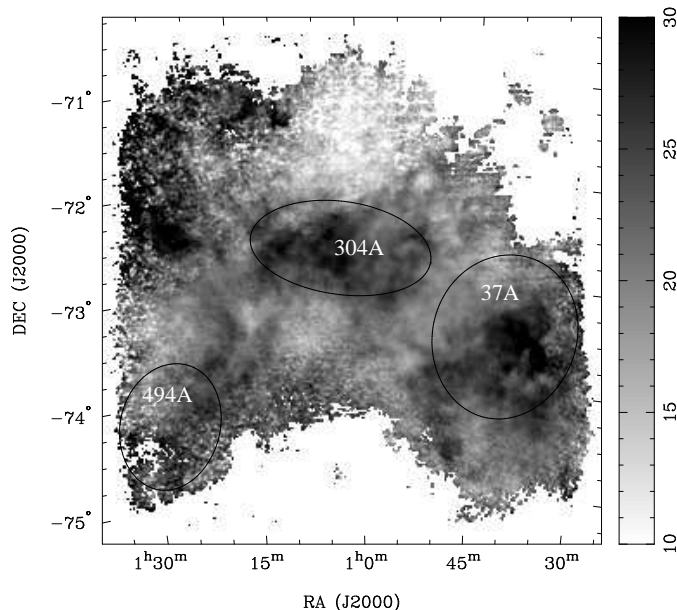


FIG. 4.— The velocity dispersion of the SMC from the second moment analysis obtained from the combined ATCA and Parkes data cube. The grey-scale range is 6 to 37 km s^{-1} . Positions of the three largest shells (37A, 304A and 494A) from Stanimirović et al. (1999) are overlaid. All pixels with a corresponding HI column density lower than 7×10^{20} atoms cm^{-2} were masked out.

(1994) and Kroupa & Bastian (1997). At any position across the SMC the proper-motion corrected heliocentric velocity was obtained by subtracting the projection of the heliocentric transverse velocity of the center of the SMC on the line-of-sight from the observed radial heliocentric velocity. The values for the conversion between the observed and the proper-motion corrected heliocentric velocity range between -23 km s^{-1} , in the north-west, and 28 km s^{-1} , in the south-east. The correction for the proper motion, however, did not make as big difference as in the case of the LMC (Luks & Rohlfs 1992). The reason is that the angular extent of the SMC is less than half that of the LMC. In addition, the direction of the SMC’s motion is perpendicular to the observed velocity gradient resulting in the gradient being almost unaffected by the proper motion.

(ii) Velocity profiles in the SMC are usually very complex, having double or even multiple-peak components. Since the intensity-weighted mean velocity (Fig. 3) is biased towards the velocity component with higher intensity, it is not necessarily the best representation of complex velocity profiles. To avoid this bias, we found, for each line-of-sight, the minimum and maximum velocity for which the intensity is 5% of the peak value for that line-of-sight. The mean of the minimum and maximum velocity, determined in this way, was then taken to be our new velocity estimate. Since such an analysis requires a high signal-to-noise ratio, we only used the low resolution Parkes data cube. The resultant velocity field has a more regular ‘spider’ pattern than the mean one, however irregularities are still present in the north and close to the Eastern Wing region. We also investigated the existence of a bimodal velocity field, by modeling each velocity profile in the Parkes data cube with one or a superposition of two independent Gaussian functions. As a result, two separate velocity structures were depicted, with central velocities corresponding to the low and high velocity entities

of 137 km s^{-1} and 174 km s^{-1} , respectively. The position-velocity diagrams show almost parallel velocity fields of these two components. However, in many cases the velocity fields intersect suggesting that two separate velocity components may be a consequence of the statistical data handling of complex HI profiles with no substantial physical meaning.

The proper-motion corrected velocity field in the Galactocentric velocity reference frame, derived from the Parkes HI data cube using the 5% cut-off described in (ii), is shown in Fig. 5. A clear velocity gradient is noticeable from -15 km s^{-1} , in the south-west, to 53 km s^{-1} , in the north-east. The positions of the three largest shells in the SMC are also overlaid in Fig. 5, suggesting that super-shells 304A and 494A may still be responsible for some of the perturbations in the velocity field. Some perturbations are also visible in the north-west.

3.3. Comparison with other tracers

3.3.1. SMC morphology from stellar populations

It has been known for some time that young and old stellar populations in the SMC have significantly different spatial distributions (e.g. Gardiner & Hatzidimitriou (1992)). Several recent stellar surveys have especially enhanced our knowledge about the different morphological properties of different stellar populations. The recent stellar survey of the central SMC ($4^\circ \times 4^\circ$) by Zaritsky et al. (2000) showed that while young stars (with ages $\lesssim 200$ Myr) exhibit an irregular distribution, similar to that seen in HI, the old stellar population (with ages $\gtrsim 1$ Gyr) shows regular, undisturbed, and almost spheroidal distribution. Similar results were reached from the DENIS survey by Cioni et al. (2000) based on IJK_s IR bands. These studies also pointed out that the ‘bar’ and the Eastern Wing region may not be distinct dynamical entities, but could be a result of recent hydrodynamic interactions between the LMC and SMC’s gaseous components. Maragoudaki

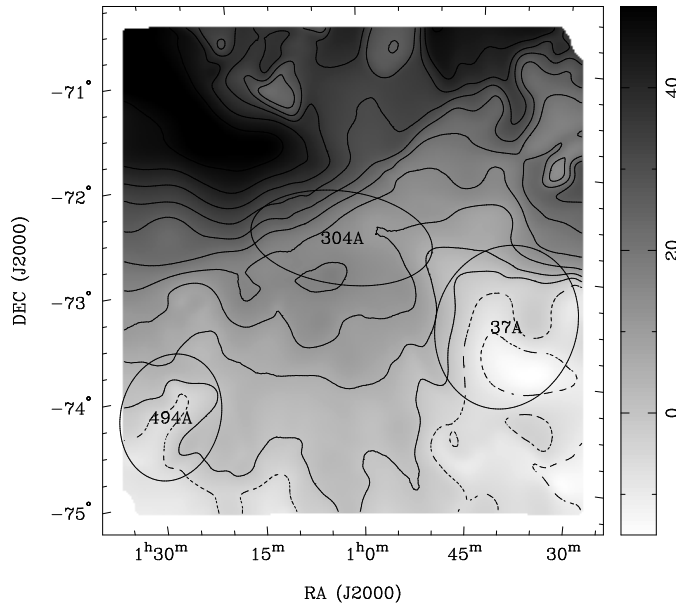


FIG. 5.— The galactocentric velocity field of the SMC, from the Parkes HI observations, with angular resolution of ~ 15 arcmin, corrected for the proper motion. The grey-scale range is -15 to 50 km s^{-1} with a linear transfer function. The contour levels range from -20 to 50 km s^{-1} , with an interval of 5 km s^{-1} . The three largest supershells (37A, 304A and 494A) from Stanimirović et al. (1999) are superimposed.

et al. (2001) further investigated the dynamical origin of the ‘bar’ by using isodensity contour maps of stars with different ages. They found similar results concerning old stellar populations. In addition, their data show that the ‘bar’ and the Eastern Wing region were already prominent features some 0.3–0.4 Gyr ago; however, it is not clear whether this is a temporary extended region of star formation or a genuine, dynamical feature.

3.3.2. SMC kinematics from stellar populations

The intermediate age and old stellar populations, traced by planetary nebulae (Dopita et al. 1985) and carbon stars (Hardy et al. 1989; Hatzidimitriou et al. 1997; Hatzidimitriou 1999; Kunkel et al. 2000), do not show signs of rotation. The red horizontal branch clump stars in the north-east show a velocity gradient of 70 km s^{-1} which was interpreted as due to a distance spread of 10 kpc along the line-of-sight (Hatzidimitriou et al. 1993). The young stellar population, traced by HI shells, shows a clear velocity gradient from the south-west to the north-east (Staveley-Smith et al. 1997), while Cepheids may have a similar trend with velocity (Mathewson et al. 1988). All populations show similar mean heliocentric velocity and velocity dispersion regardless of age and location (Hatzidimitriou 1999; Staveley-Smith et al. 1997).

From an analysis of 150 carbon stars, Kunkel et al. (2000) estimated the inclination of the SMC orbital plane to $i = 73^\circ \pm 4^\circ$ relative to the plane of the sky. They found that carbon stars are associated with more negative velocity and denser HI, while low density HI seems to be devoid of carbon stars. This suggests that non-gravitational forces must be acting on the gaseous component to provide its separation from stellar systems. Similar estimates for the SMC’s inclination were reached using Cepheids by Caldwell & Coulson (1986), $i = 70^\circ \pm 3^\circ$, and by Groenewegen (2000), $i = 68^\circ \pm 2^\circ$.

4. THE 3-D STRUCTURE OF THE SMC

4.1. Previous observational models

The 3-D structure of the SMC has been a matter of great controversy in the past. Since early mapping of HI, complex HI profiles pointed to the existence of unusual motions of the gas (Hindman 1967). Hindman (1967) also suggested the first model of the SMC, as a flattened disk with three supergiant shells in the main body.

From the analysis of the radial velocity distributions of HI, stars, HII regions, and planetary nebulae, Mathewson & Ford (1984) and Mathewson, Ford & Visvanathan (1986, 1988) suggested the ‘two separate entities’ model for the SMC, whereby the SMC is, along most of its angular extent, broken into two velocity subsystems (the Small Magellanic Cloud Remnant, SMCR, and the Mini Magellanic Cloud, MMC). In this model, the SMCR and MMC are separated in velocity by ~ 40 km s^{-1} , and have their own nebular and stellar populations. The reason proposed for this disruption of the SMC was its close encounter with the LMC some 2×10^8 yr ago. A slight modification of the ‘two separate entities’ model was suggested by Torres & Carranza (1987), and Martin et al. (1989), who found four, instead of two, different velocity components.

Caldwell & Coulson (1986) also used Cepheids to suggest the ‘bar and three arms’ geometrical model of the SMC. The central bar is very elongated (5-to-1) and is seen edge-on. A distant arm of material is pulled from the center of the SMC to the west, while two sides of the bar located in the north-east and the south-west are considered as two near arms.

4.2. Depth along the line-of-sight

The question of the 3-D structure of the SMC is closely related to the long-standing and greatly controversial issue of the SMC’s depth along the line-of-sight. By measuring distances and radial velocities of 161 Cepheids, Mathewson et al. (1986) found a great depth along the line-of-sight of ~ 30 kpc, and a distance gradient from the

north-east to the south-west. The large depth of the SMC was supported later by Mathewson et al. (1988), using Cepheids again, and by Hatzidimitriou & Hawkins (1989) and Hatzidimitriou et al. (1993) from a study of the intermediate-age (halo) population.

Welch et al. (1987) have pointed out that the determination of the Cepheid distances in Mathewson et al. (1986) suffers from a few possible problems: an inconsistent correction to mean magnitude, the assumption of zero intrinsic scatter for the period-luminosity (P-L) relation, and sample inhomogeneity. Welch et al. (1987) concluded that the SMC does not extend in depth beyond its tidal radius (4 – 9 kpc). Martin et al. (1989) confirmed that the young stars in the SMC lie within a depth of < 10 kpc. On the other hand, Groenewegen (2000) used near-infrared observations of Cepheids, which are less affected by reddening and metallicity, and derived the depth of the SMC of 14 kpc, assuming that the P-L relation has the same scatter for both the LMC and the SMC.

Although Cepheids are used as the main distance indicators, the P-L relation requires an independent zero-point calibration, which is very difficult to achieve, and could suffer from a significant metallicity dependence. Another source of error in the distance determination, that has not been previously fully appreciated, is differential extinction toward the SMC. While reddening of Cepheids in the SMC has been extensively studied (see Welch et al. (1987) for a summary), a constant value has been often applied for distance determination. For example, Mathewson et al. (1986) found no sign of differential reddening and assumed a uniform correction of 0.06 mag for their sample of 161 Cepheids.

Recently, Zaritsky et al. (2002) determined the extinction map across the SMC, using the Magellanic Clouds Photometric Survey, and showed that extinction varies both spatially across the SMC and with stellar population. They found that young, hot stars have an average extinction 0.3 mag higher than old, cool stars, and that young stars show a significant increase in extinction along the main SMC ridge, from the north-east to the south-west. Zaritsky et al. (2002) found $E_{B-V} \sim 0.05 - 0.25$ mag. For comparison, the mean value for the interstellar reddening previously measured by Caldwell & Coulson (1985) was $E_{B-V} = (0.054 \pm 0.021)$ mag, while Sasselov et al. (1997) found a slightly higher value of $E_{B-V} = (0.125 \pm 0.009)$ mag.

The differential extinction across the SMC has a significant influence on the distance estimate. Differential reddening toward Cepheids in the south-west part of the SMC is ~ 0.2 mag higher than toward in the north-east. This results in the interstellar infrared absorption being larger in the south-west by ~ 0.4 mag. Hence, the Cepheid distances estimated by Mathewson et al. (1988) could be over-estimated by up to 18%. This corresponds to about 10 kpc at a distance of 60 kpc, and suggests that the correction for the interstellar absorption can significantly influence the distance determination, and easily bring the depth of the SMC within its tidal radius (4 – 9 kpc).

5. COMPARISON WITH THEORETICAL MODELS

There are two families of theoretical models, based on either a tidal or a ram pressure scenario, that try to re-

produce observational features in the Magellanic System, caused by interactions between the SMC, LMC, and the Galaxy. The 3-D structure and kinematics of the SMC were particularly addressed in tidal models by Gardiner et al. (1994), Gardiner & Noguchi (1996), and Yoshizawa & Noguchi (2003). The recent work by Yoshizawa & Noguchi (2003) provides, to date, the most detailed model for the evolution of the SMC. We summarize here results from these tidal simulations and their major predictions concerning the structure and kinematics of the SMC.

It is important to note that none of the theoretical models so far predicts the bimodal velocity distribution throughout the main gaseous body of the SMC. This gives support to the idea that most, if not all, of the observed line-splitting comes from the combined effects of numerous expanding shells (Staveley-Smith et al. 1997).

5.1. Model predictions

The above three models come from N-body simulations of the gravitational interactions in the Galaxy-LMC-SMC system to reproduce the observed gas distribution in the Magellanic System, primarily those of the Magellanic Stream and Bridge. While Gardiner et al. (1994) modeled the SMC as a single-component disk-like system, in simulations by Gardiner & Noguchi (1996) the SMC was represented by a two-component particle system consisting of a nearly spherical halo and a rotationally supported disk, with a disk-to-halo mass ratio of 1:1. This high mass ratio resulted in the original disk quickly becoming unstable, and being transformed into a bar-like structure. The tidal model by Yoshizawa & Noguchi (2003) included, for the first time, gas dynamics and star formation processes, while representing the SMC also as a rotationally supported exponential disk with a nearly spherical halo, having the disk-to-halo mass ratio of 3:7. The significantly lower disk mass resulted in the disk being stable against bar instabilities. Following typical findings for the Magellanic-type galaxies, a slowly rising rotation curve was assumed in both models, with a turnover radius of 3.5 kpc and maximum rotation velocity of 50 km s⁻¹. The best spatial orientation of the original SMC disk was determined in Gardiner & Noguchi (1996) to have an inclination $i = 45^\circ$ and major axis $\theta = 230^\circ$ in order to match the observed gas and stellar distributions. These values were adopted by Yoshizawa & Noguchi (2003) and simulations were repeated for different star formation parameters.

The major and common result of all three models is that the current 3-D structure of the SMC is composed of a central, disk- or bar-like, component and two tidal, spiral-arm-like tails. These tidal tails extend into the Magellanic Bridge, were formed 200 Myr ago, and are seen in both gas and stellar components. In particular, simulations by Yoshizawa & Noguchi (2003) show great morphological change of the initial SMC's gas disk – from its original size of about 10 kpc in diameter the disk shrunk forming first the Magellanic Stream and the Leading Arm (about 1.5 Gyr ago), and then later two tidal arms that form the Magellanic Bridge (about 200 Myr ago). At the end of the simulation the gas disk is still present but is now significantly smaller in size, approximately by a factor of 2.5. The current SMC consists of the following components.

1. The left-over **disk-like component**, located at

$0^{\text{h}}15^{\text{m}} < \text{RA} < 1^{\text{h}}$, is not greatly elongated along the line-of-sight, with the stellar disk having a higher distance dispersion than the gas disk. Kinematically, the gas disk has a significant velocity gradient, from ~ 80 to 180 km s^{-1} . The left-over stellar disk, on the other hand, shows high dispersion in the velocity field but no significant velocity gradient. In simulations by Gardiner & Noguchi (1996), this is a bar-like feature slightly bigger and centered more westward, covering $0^{\text{h}}30^{\text{m}} < \text{RA} < 1^{\text{h}}30^{\text{m}}$, and a slightly wider velocity range.

2. The **eastern tail**, starting around $\text{RA} \sim 1^{\text{h}}$, extending into the Magellanic Bridge, and covering a distance range from 55 to 40 kpc. This feature starts at a heliocentric velocity of about 170 km s^{-1} and gradually decreases to about 120 km s^{-1} at $\text{RA} > 2^{\text{h}}$. It is seen in both gas and stars but the gas tail is more extended.
3. The **western tail**, starting around $\text{RA} \sim 0.5^{\text{h}}$ and covering a distance range from 55 to almost 80 kpc. Kinematically, this feature starts westward from the main disk-like component at a velocity of about 80 km s^{-1} , but then turns east passing the main component with increasing velocity all the way to about $> 250 \text{ km s}^{-1}$ around $\text{RA} > 2^{\text{h}}$. The stellar western tail follows the gas one and is less extended.

Hence, the two tidal tails contribute mostly to the SMC's elongation along the line-of-sight, while the SMC disk-like component is not significantly elongated (~ 5 kpc).

The best simulation by Yoshizawa & Noguchi (2003) reproduces a large number of observational properties in the Magellanic System, suggesting that most of them may be predominantly of tidal origin. Very importantly, a good morphological and kinematic reproduction of the Magellanic Stream with almost no stars was achieved for the first time, by using a very compact initial configuration of the SMC's stellar disk. The major shortcoming of the model is its failure to reproduce gas masses and mass ratios in the Magellanic Stream, Bridge, and the SMC. This may be related with the need for a more massive initial disk of the SMC, or a different halo-to-disk mass ratio, and requires further investigation. In addition, as pointed out by Putman et al. (2003), a number of detailed features related to the Magellanic Stream (e.g. its double-helix appearance and numerous small clouds surrounding its main filaments) need to be explained. It has also been shown that forces other than gravity must play a significant role in the kinematics of the SMC (Kunkel et al. 2000; Zaritsky et al. 2000).

The results of tidal numerical simulations show that the current central gaseous body of the SMC (~ 4 degrees in extent) has a significant velocity gradient. Gardiner & Noguchi (1996) explained this gradient as being due to the elongation of the SMC's bar-like component along the line-of-sight. However, a significant angular momentum left from before the last two close encounters with the LMC is expected to be present, if the pre-encounter SMC disk had an internal spin. The N-body simulations by Mayer

et al. (2001) showed that in general disk-like dwarf irregular galaxies undergo a great morphological transformation due to close encounters with the more massive Milky Way. While dwarfs lose their mass through tidal stripping, their angular momentum gets gradually removed over a period of 6-10 Gyrs. This transformation is gradual, and on short timescales (~ 2 Gyrs) a significant angular momentum ($> 80\%$) is still preserved. Focusing especially on the SMC case, a similar conclusion was reached by Kunkel et al. (2000) who found that it is extremely hard for the SMC to lose its pre-encounter angular momentum during an encounter with the LMC.

5.2. Comparison with HI

In Section 3.2 we showed that the HI distribution contains a large velocity gradient and some signatures for the existence of ordered, systematic motions. This agrees with theoretical simulations which show that the current central gaseous body of the SMC should still possess angular momentum left over from before the last two close encounters with the LMC. This angular momentum should be less significant in the case of older stellar populations, as indeed has been found from observations (see Section 3.3 for a summary). We now compare RA-velocity slices through the HI data cube, shown in Fig. 6, with the theoretical predictions, shown in Fig. 17 of Yoshizawa & Noguchi (2003) and Fig. 10 of Gardiner & Noguchi (1996). The area enclosed in our observations contains only the central region of the SMC ($4.5^\circ \times 4.5^\circ$).

Images in Fig. 6 show coherent large-scale features with a wealth of small-scale structure. Many of the features have already been interpreted as expanding shells of gas (Staveley-Smith et al. 1997; Stanimirović et al. 1999). At a low Dec of $\sim -74^\circ$, the two most dominant features are supergiant shells 37A (RA $01^{\text{h}} 25^{\text{m}}$) and 494A ($00^{\text{h}} 35^{\text{m}}$). These shells were investigated in Stanimirović et al. (1999). Around Dec $\sim -73^\circ 20'$, Fig. 6 shows an HI emission, bar-like, feature stretching over the RA range $00^{\text{h}} 40^{\text{m}}$ to $\sim 00^{\text{h}} 55^{\text{m}}$, and having a velocity gradient from ~ 120 to $\sim 170 \text{ km s}^{-1}$. This feature continues eastward as a complex network of filaments and shell-like features, culminating around Dec $\sim -72^\circ 37'$ with two long filaments centered at heliocentric velocities of 130 and 170 km s^{-1} . The coherent appearance of these features traced throughout the data cube was interpreted as the low-Dec hemisphere of the supergiant shell 304A (see Stanimirović et al. 1999). At a very high Dec of $\sim -71^\circ 55'$, a high-velocity component is apparent, at about 200 km s^{-1} .

We do not find obvious features that could correspond to the predicted eastern and western tails within the region covered by our observations. To search for potential tidal tails running out of the central SMC main body an investigation of a larger area is essential; this will be possible in the near future with new observations by Brüns et al. (2002) and Muller et al. (2003), but is beyond the scope of this paper. Concerning the position and velocity range of the central component, our observations are in better agreement with the Gardiner & Noguchi (1996) model predictions: the coherent structure seen from RA $00^{\text{h}} 30^{\text{m}}$ to $01^{\text{h}} 30^{\text{m}}$ corresponds to the area where the central bar-like feature predicted by the model should be found, and its velocity span from 100 to 200 km s^{-1} is

FIG. 6.— [f6.jpeg] Ten RA-velocity slices through the combined ATCA and Parkes HI data cube of the SMC, starting with Dec $-74^{\circ}42'12''$ and ending with Dec $-72^{\circ}17'42''$ (J2000). The grey-scale range is: 0–45, 0–45, 0–55, 0–75, 0–75, 0–75, 0–75, 0–55, 0–45, 0–45 K respectively, with a linear transfer function.

FIG. 7.— [f7.jpeg] *continued from Fig. 6*

very close to the predicted velocity range for the bar-like component. The Yoshizawa & Noguchi (2003) model predictions for the left-over disk component cover a smaller area and velocity range than what is found in the observations.

6. ROTATION CURVE AND MASS MODELING OF THE SMC

As discussed in the previous section, the central $4^{\circ} \times 4^{\circ}$ of the SMC, covered by the HI observations, most likely corresponds to the left-over part of the original SMC's gaseous rotationally supported disk. This disk should contain significant signatures of angular momentum left from the pre-encounter disk. Motivated by this, we proceed further to derive the rotation curve from the observed HI velocity field, and the mass model, assuming that the entire velocity gradient is due to rotation.

6.1. Tilted ring analysis

The velocity field derived in Section 3.2, and shown in Fig. 5, was used to define the major and minor kinematic axes, and the apparent kinematic center at \sim RA $01^{\text{h}}05^{\text{m}}$, Dec $-72^{\circ}25'$ (J2000), with a systemic velocity of ~ 20 km s $^{-1}$ in the galactocentric reference frame. The position angle (PA) of the major kinematic axis is around 50° . The tilted ring algorithm ROCUR in the AIPS package was then used to derive the HI rotation curve at different radii from the center. A fairly standard procedure (Meurer et al. 1998; Bureau & Carignan 2002) was applied to estimate a set of kinematic parameters that represents well the observed velocity field at all radii. It was found that solutions for the inclination vary greatly especially for the outer radii. In the end, the value $i = 40^{\circ} \pm 20^{\circ}$ was adopted. The newly determined least-squares solution for the systemic velocity was found to be 24 km s $^{-1}$. Finally, the solutions for the rotational velocity and position angle were determined and are shown in Fig. 8. The position angle varies systematically from 30° to 50° (as shown in the top panel of Fig. 8). Using the mean PA, the global and the separate rotation curves for the receding and approaching sides of the velocity field were derived, as shown in Fig. 8 (bottom panel).

The global rotation curve shows a slow rise up to $R \sim 3$ kpc, where it reaches the maximum velocity of ~ 40 km s $^{-1}$. The receding and approaching curves are significantly different, which is not surprising since the velocity field is quite asymmetric (Fig. 5). The receding curve is less smooth and could have a local maximum around 1 kpc from the center of rotation. The maximum rotation velocity found in previous studies (Hindman 1967; Loiseau & Bajaja 1981) was ~ 36 km s $^{-1}$.

The line-of-sight HI velocity dispersion distribution shown in Fig. 4 pointed to a high velocity dispersion across most of the SMC. The mean value, $\sigma_{\text{HI}} = (22 \pm 2)$ km s $^{-1}$, is significantly higher than what is found for spiral galaxies, or even other dwarf galaxies (Meurer et al. 1998; Côté

et al. 2000). It is also large compared to the rotational velocity (Fig. 8). If interpreted as being all due to random motions, rather than bulk motions along the line-of-sight, such high values for σ_{HI} suggest that the turbulence in the ISM of the SMC has an important influence on the system dynamics.

To account for this dynamical support we estimated the asymmetric drift correction. The usual prescription for determining this correction (Meurer et al. 1996) was followed: we derived the azimuthally averaged HI surface brightness and velocity dispersion profiles (for deprojected circular annuli with a mean position angle of 40° and an inclination of 40°), and assumed a constant vertical scale height. In general, the derived asymmetric drift correction is quite significant and range from 0, for the inner radii, to ~ 40 km s $^{-1}$ for the outer radii. The observed rotation curve corrected for the pressure support is presented in Fig. 9 (crosses). The difference is significant for $R > 0.5$ kpc with the corrected curve being higher by ~ 10 km s $^{-1}$ than the observed one.

6.2. The mass model

A two-component mass model was fitted to the corrected rotation curve.

(a) To derive the deprojected rotation curve due to the potential resulting from the neutral gas alone, the radial HI surface density profile was used in the GIPSY's ROTMOD task (van der Hulst et al. 1992). An exponential density law was assumed for the vertical disk distribution, with a scale height of 1 kpc. An indication of the large scale height was given by the typical size of large HI shells in the SMC, as well as from previous estimates based on the velocity dispersion and an average surface density of matter for the case of an isothermal disk. The resultant rotation curve (V_{g}) is shown in Fig. 9 with dotted line.

(b) To derive the deprojected rotation curve due to the optical surface density distribution, the V-band image (shown in Fig. 2) was used. This image was first smoothed to 20 arcmin resolution and scaled to match the total luminosity of the SMC in the V-band of $3.1 \times 10^8 L_{\odot}$ (de Vaucouleurs et al. 1991). The rotation curve arising from the stellar potential alone (V_{*}) was estimated from the V-band stellar density profile assuming, in first approximation, that $M_{*}/L_{\text{V}} = 1$ (see the curve shown as a dash-dotted line in Fig. 9). The best fit of the total predicted rotational velocity, $\sqrt{V_{\text{g}}^2 + V_{*}^2}$, to the observed rotational velocity corrected for the pressure support was obtained for $M_{*}/L_{\text{V}} = 1.02$ (solid line in Fig. 9). The two component mass model appears to fit the observed rotational velocities quite well, suggesting that no additional component, such as a dark halo, is needed to explain the rotation of the SMC.

The rotation velocity of only the stellar component implies a total stellar mass of the SMC of $1.8 \times 10^9 M_{\odot}$, within a radius of 3 kpc. From Section 2 and after correc-

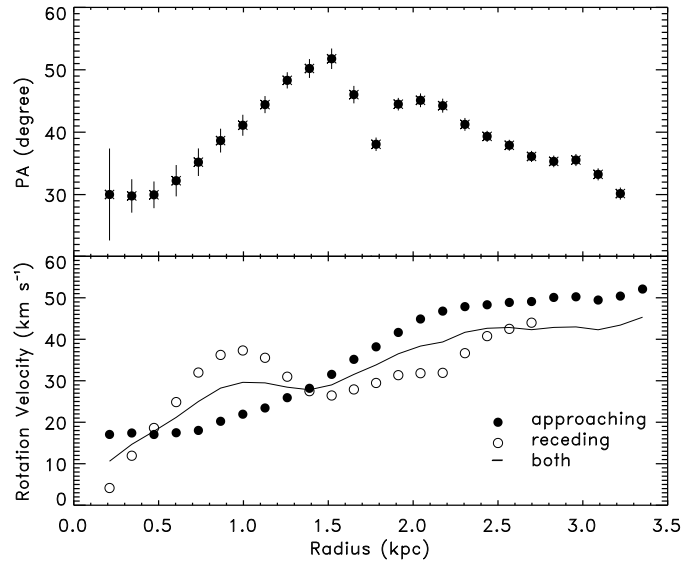


FIG. 8.— The least-squares solution for the position angle (PA) of the kinematic line of nodes (top panel) and the rotational velocity (V_{Rot}) (bottom panel) as a function of radius. The mean position angle is 40° . The rotation curves for the approaching and receding sides of the velocity field are shown with filled and open circles, respectively. The global rotation curve is shown with the solid line.

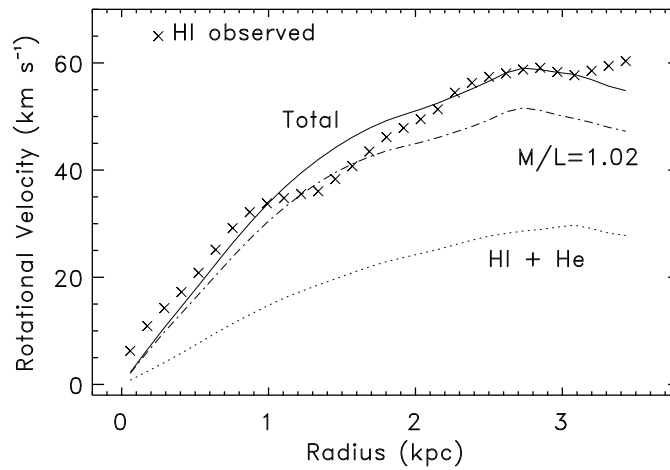


FIG. 9.— The observed rotation curve, corrected for the pressure support (crosses), compared with the total predicted rotation curve (solid line), composed of: (a) the gaseous, HI+He, component (dotted line); (b) the stellar component (dash-dotted line) with an estimated mass-to-light ratio $M_*/L_V = 1.02$.

tion for neutral He, the mass of HI+He is $5.6 \times 10^8 M_\odot$, being almost a third of the stellar mass within the same radius. The total mass of the SMC, implied from the rotation curve, is thus $2.4 \times 10^9 M_\odot$. This is almost twice that of $1.5 \times 10^9 M_\odot$, derived by Hindman (1967) within the slightly smaller radius of 2.6 kpc, and is similar to the initial mass of the SMC assumed by Gardiner et al. (1994) (about $2 \times 10^9 M_\odot$) and by Yoshizawa & Noguchi (2003) ($3 \times 10^9 M_\odot$).

6.2.1. The stellar M/L from population synthesis models

Stellar population synthesis (SPS) models provide an independent way to estimate the stellar mass-to-light ratio. Bell & de Jong (2001) used simplified spiral galaxy evolution models, based on several different SPS models, to investigate trends of the stellar M/L with galaxy properties, such as colors and gas fraction. They found good agreement with observational data and showed that the trend of M/L with color, $\log_{10}(M/L) = a_\lambda + b_\lambda \text{Color}$, is robust with respect to the SPS models but is dependent on the type of the initial mass function (IMF) used. They tabulate coefficients a_λ and b_λ for different colors, stellar metallicity, SPS models, and IMFs.

We have used coefficients for the case of a stellar metallicity appropriate for the SMC, which is about 25% of the solar abundance, based on the SPS model by Bruzual & Charlot (2003), for a Salpeter IMF scaled by a factor of 0.7 (Bell & de Jong 2001), and the Schmidt (1959) star formation law. The stellar M/L_V was then estimated using the broad band colors given in Table 1, $B - V = 0.41$ and $B - R = 0.7$. We get $M/L_V = 0.8 \pm 0.2$ which agrees with the value obtained from the HI rotation curve.

6.3. Critical density for star formation

We now go a step further and address the gravitational stability of the current gaseous disk of the SMC and its possible consequences for star formation. We estimated the disk stability parameter, Q , (Toomre 1964) using the mean velocity dispersion, azimuthally averaged HI surface brightness, and the angular velocity derived using the rotation velocity. According to the Toomre's stability criterion, the disk is stable for $Q > 1$, while regions with $Q \lesssim 1$ are unstable and under possible fragmentation which can lead to new star formation (Binney & Tremaine 1987). The estimated values of Q , as a function of radius, are shown in Fig. 10. The plot shows that most of the gaseous disk, for $R < 2.1$ kpc, is unstable and, most likely, under current star formation. The unstable region appears to be quite extended, reaching almost the cut-off $H\alpha$ radius, $R(H_\alpha) \approx 2.6$ kpc (based on $H\alpha$ observations by Kennicutt et al. (1995)), which delineates the parts of the gaseous disk under the most recent star formation.

We also determined the so called critical surface density, defined as the surface density needed to stabilize the disk (or for $Q = 1$). Both the observed (Σ_{HI}) and critical (Σ_c) surface densities are shown in Fig. 11 (top panel). The ratio of the observed to critical surface density ($\alpha = \Sigma_{\text{HI}}/\Sigma_c = 1/Q$) is shown in the same figure (bottom panel). For the unstable part of the disk, α varies between 1.0 and 2.0, while it has a constant value of $\alpha = 0.74 \pm 0.04$ for the stable part of the disk. This agrees with the empirical relationship between the star formation threshold and

the disk stability found by Kennicutt (1989) for a sample of normal galaxies, whereby most of the star formation is taking place for $\alpha > 0.67$ (and hence for $Q < 1.5$).

7. SUMMARY AND CONCLUDING REMARKS

We have used the latest HI observations, obtained with the ATCA and the Parkes telescope, to re-examine the kinematics of the SMC. The HI velocity field, derived in Section 3.2, shows a large velocity gradient from the south-west to the north-east. The iso-velocity contours of this velocity field show some symmetry, suggestive of a differential rotation. Some large-scale distortions in this velocity field are easily visible, but could be related to positions of several supergiant shells. In contrast to the HI distribution, the old stellar populations appear to have a spheroidal spatial distribution and a total absence of rotation. In Section 4, we summarized previous observational models of the SMC and the greatly controversial issue of its possibly large depth along the line-of-sight. We cautioned that the differential extinction across the SMC, revealed recently by Zaritsky et al. (2002), could be a significant source, unappreciated previously, for an overestimate of stellar distances, and therefore the SMC's depth.

In Section 5, we summarized several tidal models that are concerned with the 3-D structure and kinematics of the SMC. In order to reproduce observational characteristics of the Magellanic System these models needed to assume the existence of angular momentum in the pre-encounter SMC (about 1.5–2 Gyr ago). Models predict that the current, left-over material from the pre-encounter SMC disk is a disk-like or a bar-like feature, about 4 kpc in extent, with a velocity gradient of about 100 km s^{-1} . This velocity gradient is at least partially from the original angular momentum, as it is very difficult to lose the original spin during a galaxy encounter (Mayer et al. 2001; Kunkel et al. 2000). The elongation along the line-of-sight of the pre-encounter SMC disk may also be partially responsible. It is, however, not clear from the models what are the relative contributions of these two effects to the predicted velocity gradient. In addition, theoretical models predict higher velocity dispersion for the post-encounter stellar disk without a significant velocity gradient; this agrees with observations of older stellar populations summarized in Section 3.3.2.

While we do not find evidence for the existence of tidal tails predicted by the models, the central region of the SMC covered in these observations most likely corresponds to the central component left-over from the pre-encounter SMC gaseous (rotationally supported) disk. The observed HI velocity gradient agrees well with the model predictions. We then proceeded further to derive its rotation curve and mass model in Section 6. A set of kinematic parameters derived from the tilted ring analyses agrees extremely well with the assumptions used in theoretical models that led to a good reproduction of observational properties of the Magellanic System. The derived HI rotation curve in Section 6 rapidly rises to about 60 km s^{-1} up to the turnover radius of ~ 3 kpc. A stellar mass-to-light ratio of about unity was required to scale the stellar component of the SMC's rotation curve to match the observed rotation curve. This suggests that a dark matter halo is not needed to explain the dynamics of the SMC. This is a surprising result, as dwarf irregular galaxies are often

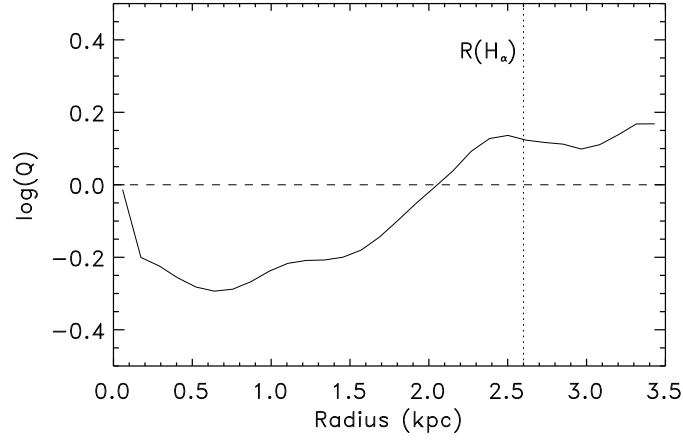


FIG. 10.— Radial variation of Toomre’s disk stability parameter Q . The dashed line shows $Q = 1$ which separates disk-stable ($Q > 1$) from disk-unstable phase ($Q < 1$). The radius where the $H\alpha$ profile departs from an exponential distribution, at approximately $R(H\alpha) = 2.6$ kpc, is shown with a dotted line.

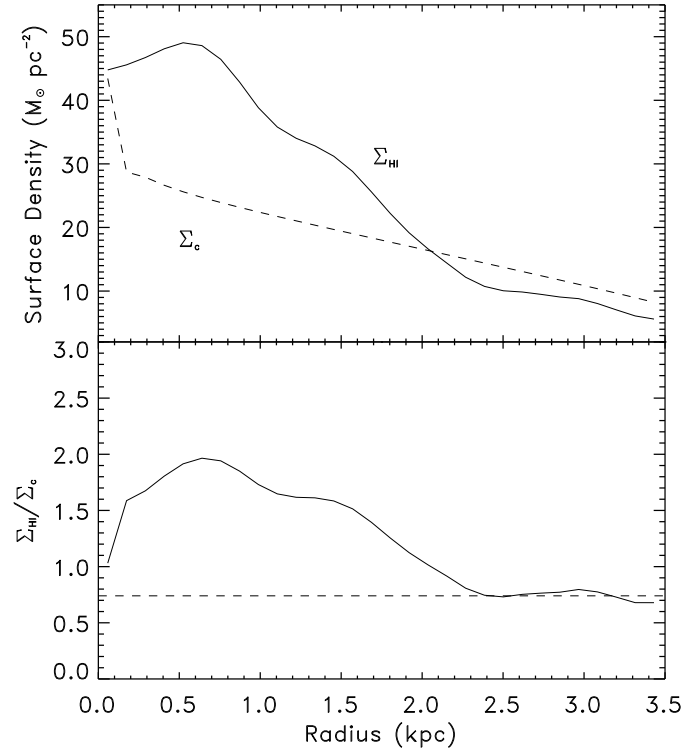


FIG. 11.— Top panel: the radial distribution of the observed (Σ_{HI}) and critical (Σ_c) surface density of the gas in the SMC. Bottom panel: the radial distribution of the ratio of the observed to the critical surface density ($\alpha = \Sigma_{\text{HI}}/\Sigma_c$). The dashed line shows $\alpha = 0.74$.

found to be dark matter dominated, and could be related to the mechanism of tidal stripping, as indicated by Mayer et al. (2001). The total dynamical mass of the SMC derived from the rotation curve is $2.4 \times 10^9 M_{\odot}$, three quarters of which are due to the stellar mass only. We also derived Toomre's disk stability parameter Q , which shows that almost all of the SMC disk is in the unstable regime. The gravitationally stable part, on the other hand, has a ratio of the observed to critical surface density $\alpha = 0.74$ which is in excellent agreement with the empirical stability threshold found by Kennicutt (1989).

All of the above suggest that the HI distribution is capable of providing valuable information about the SMC dynamics. Although very disturbed, it still contains imprints of the original system prior to the latest encounters with the LMC and the Galaxy. The HI data discussed here comprise only the central $4.5^{\circ} \times 4.5^{\circ}$ of the SMC. It is very important to compare tidal theoretical models with data comprising a larger area around the SMC to search

for signatures of the proposed tidal tails. This will be possible in the near future using the Parkes Multibeam HI observations of the whole Magellanic System (Brüms et al. 2000), as well as the ATCA and Parkes observations of the Magellanic Bridge (Muller et al. 2003).

The HI SMC data set is available from the ATNF SMC web page (http://www.atnf.csiro.au/research/smc_h1/).

ACKNOWLEDGMENTS

We are greatly thankful to Mike Bessell for providing us with the V-band optical image of the SMC prior to publication. We thank Greg Bothun for sending us the H α image. We thank John Dickey, Jacco van Loon, and Mary Putman for stimulating and fruitful discussions, and an anonymous referee for insightful comments. This work was supported in part by NSF grants AST-0097417 and AST-9981308.

REFERENCES

- Bajaja, E. & Loiseau, N. 1982, *A&AS*, 75, 251
 Bell, E. F. & de Jong, R. S. 2001, *ApJ*, 550, 212
 Binney, J. & Tremaine, S. 1987, *Galactic dynamics* (Princeton, New Jersey: Princeton University Press), 362
 Brüms, C., Kerp, J., & Staveley-Smith, L. 2002, in *ASP Conf. Ser.* 276: Seeing Through the Dust: The Detection of HI and the Exploration of the ISM in Galaxies, 365
 Brüms, C., Kerp, J., & Staveley-Smith, L. 2000, in *ASP Conf. Ser.* 218: Mapping the Hidden Universe: The Universe behind the Milky Way - The Universe in HI, 349
 Bruzual, G. & Charlot, S. 2003, *MNRAS*, 344, 1000
 Bureau, M. & Carignan, C. 2002, *AJ*, 123, 1316
 Côté, S., Carignan, C., & Freeman, K. C. 2000, *AJ*, 120, 3027
 Caldwell, J. A. R. & Coulson, I. M. 1985, *MNRAS*, 212, 879
 —. 1986, *MNRAS*, 218, 223
 Cioni, M.-R. L., Habing, H. J., & Israel, F. P. 2000, *A&A*, 358, 9
 de Vaucouleurs, G., de Vaucouleurs, A., Corwin, H. G., Buta, R. J., Paturel, G., & Fouque, P. 1991, *Third reference catalogue of bright galaxies* (New York: Springer-Verlag)
 Dopita, M. A., Ford, H. C., Lawrence, C. J., & Webster, B. L. 1985, *ApJ*, 296, 390
 Gardiner, L. T. & Hatzidimitriou, D. 1992, *MNRAS*, 257, 195
 Gardiner, L. T. & Noguchi, M. 1996, *MNRAS*, 278, 191
 Gardiner, L. T., Sawa, T., & Fujimoto, M. 1994, *MNRAS*, 266, 567
 Groenewegen, M. A. T. 2000, *A&A*, 363, 901
 Hardy, E., Suntzeff, N. B., & Azzopardi, M. 1989, *ApJ*, 344, 210
 Hatzidimitriou, D. 1999, in *IAU Symp.* 190: New Views of the Magellanic Clouds, 299
 Hatzidimitriou, D., Cannon, R. D., & Hawkins, M. R. S. 1993, *MNRAS*, 261, 873
 Hatzidimitriou, D., Croke, B. F., Morgan, D. H., & Cannon, R. D. 1997, *A&AS*, 122, 507
 Hatzidimitriou, D. & Hawkins, M. R. S. 1989, *MNRAS*, 241, 667
 Hindman, J. V. 1967, *Aust. J. Phys.*, 20, 147
 Hindman, J. V., McGee, R. X., Carter, A. W. L., Holmes, E. C. J., & Beard, M. 1963, *Aust. J. Phys.*, 16, 552
 Kennicutt, R. C., Bresolin, F., Bomans, D. J., Bothun, G. D., & Thompson, I. B. 1995, *AJ*, 109, 594
 Kennicutt, R. C. J. 1989, *ApJ*, 344, 685
 Kerr, F. J., Hindman, J. V., & Robinson, B. J. 1954, *ApJ*, 7, 297
 Kim, S., Dopita, M. A., Staveley-Smith, L., & Bessell, M. S. 1999, *AJ*, 118, 2797
 Kim, S., Staveley-Smith, L., Dopita, M. A., Freeman, K. C., Sault, R. J., Kesteven, M. J., & McConnell, D. 1998, *ApJ*, 503, 674
 Kroupa, P. & Bastian, U. 1997, *New Astronomy*, 2, 77
 Kroupa, P., Röser, S., & Bastian, U. 1994, *MNRAS*, 266, 412
 Kunkel, W. E., Demers, S., & Irwin, M. J. 2000, *AJ*, 119, 2789
 Loiseau, N. & Bajaja, E. 1981, *RevMexAA (Serie de Conferencias)*, 6, 55
 Luks, T. & Rohlfs, K. 1992, *A&A*, 263, 41
 Maragoudaki, F., Kontizas, M., Morgan, D. H., Kontizas, E., Dapergolas, A., & Livanou, E. 2001, *A&A*, 379, 864
 Martin, N., Maurice, E., & Lequeux, J. 1989, *A&A*, 215, 219
 Mateo, M. 1998, in *The Magellanic Clouds and Other Dwarf Galaxies*, *Proceedings of the Bonn/Bochum-Graduiertenkolleg Workshop*, held at the Physikzentrum Bad Honnef, Germany, January 19-22, 1998, ed. T. Richtler & J. Braun (Shaker Verlag, Aachen), 53-66
 Mathewson, D. S. & Ford, V. L. 1984, in *Structure and Evolution of the Magellanic Clouds*, ed. S. van den Bergh & K. de Boer, *I.A.U. Symposium No. 108* (Reidel, Dordrecht), 125
 Mathewson, D. S., Ford, V. L., & Visvanathan, N. 1986, *ApJ*, 301, 664M
 —. 1988, *ApJ*, 333, 617
 Mayer, L., Governato, F., Colpi, M., Moore, B., Quinn, T., Wadsley, J., Stadel, J., & Lake, G. 2001, *ApJ*, 559, 754
 Meurer, G. R., Carignan, C., Beaulieu, S. F., & Freeman, K. C. 1996, *ApJ*, 111, 1551
 Meurer, G. R., Staveley-Smith, L., & Killeen, N. E. B. 1998, *MNRAS*, 300, 705
 Muller, E., Staveley-Smith, L., Zealey, W., & Stanimirović, S. 2003, *MNRAS*, 339, 105
 Puche, D., Westpfahl, D., & Brinks, E. 1992, *AJ*, 103, 1841
 Putman, M. E., Gibson, B. K., Staveley-Smith, L., Banks, G., Barnes, D. G., Bhat, R., Disney, M. J., Ekers, R. D., Freeman, K. C., Haynes, R. F., Henning, P., Jerjen, H., Kilborn, V., Koribalski, B., Knezek, P., Malin, D. F., Mould, J. R., Osterloo, T., Price, R. M., Ryder, S. D., Sadler, E. M., Stewart, I., Stootman, F., Vaile, R. A., Webster, R. L., & Wright, A. E. 1998, *Nat*, 394, 752
 Putman, M. E., Staveley-Smith, L., Freeman, K. C., Gibson, B. K., & Barnes, D. G. 2003, *ApJ*, 586, 170
 Sasselov, D. D., Beaulieu, J. P., Renault, C., Grison, P., Ferlet, R., Vidal-Madjar, A., Maurice, E., Prevot, L., Aubourg, E., Bareyre, P., Brehin, S., Coutures, C., Delabrouille, N., Kat, J. D., Gros, M., Laurent, B., Lachize-Rey, M., Lesquoy, E., Magneville, C., Milsztajn, A., Moscoso, L., Queindec, F., Rich, J., Spiro, M., Vigroux, L., Zylberajch, S., Ansari, R., Cavalier, F., Moniez, M., Gry, C., Guibert, J., Moreau, O., & Tajhmady, F. 1997, *A&A*, 324, 471
 Schmidt, M. 1959, *ApJ*, 129, 243
 Stanimirović, S. & Lazarian, A. 2001, *ApJ*, 551, L53
 Stanimirović, S., Staveley-Smith, L., Dickey, J. M., Sault, R. J., & Snowden, S. L. 1999, *MNRAS*, 302, 417
 Staveley-Smith, L., Sault, R. J., Hatzidimitriou, D., Kesteven, M. J., & McConnell, D. 1997, *MNRAS*, 289, 225
 Toomre, A. 1964, *ApJ*, 139, 1217
 Torres, G. & Carranza, G. J. 1987, *MNRAS*, 226, 513
 van der Hulst, J. M., Terlouw, J. P., Begeman, K., Zwitser, W., & Roelfsema, P. R. 1992, in *ASP Conference Series*, Vol. 25, *Astronomical Data Analysis Software and Systems I*, ed. D. M. Worall, C. Biemesderfer, & J. Barnes (San Francisco: Astronomical Society of the Pacific), 131
 Walter, F. 1999, *Proc. Astron. Soc. Aust.*, 16, 106
 Welch, D. L., McLaren, R. A., Madore, B. F., & McAlary, C. W. 1987, *ApJ*, 321, 162
 Westerland, B. E. 1997, *The Magellanic Clouds* (Cambridge, United Kingdom: Cambridge University Press), 32

Yoshizawa, A. M. & Noguchi, M. 2003, MNRAS, 339, 1135
Zaritsky, D., Harris, J., Grebel, E. K., & Thompson, I. B. 2000,
ApJ, 534, 53

Zaritsky, D., Harris, J., Thompson, I. B., Grebel, E. K., & Massey,
P. 2002, AJ, 123, 855

This figure "f1.jpeg" is available in "jpeg" format from:

<http://arxiv.org/ps/astro-ph/0312223v1>

This figure "f2.jpeg" is available in "jpeg" format from:

<http://arxiv.org/ps/astro-ph/0312223v1>

This figure "f3.jpeg" is available in "jpeg" format from:

<http://arxiv.org/ps/astro-ph/0312223v1>

This figure "f6.jpeg" is available in "jpeg" format from:

<http://arxiv.org/ps/astro-ph/0312223v1>

This figure "f7.jpeg" is available in "jpeg" format from:

<http://arxiv.org/ps/astro-ph/0312223v1>